Check for updates

Tectonics

RESEARCH ARTICLE
10.1029/2020TC006260

Key Points:

- Intracrustal deformation including detached upper crust and ductile midcrustal layer was imaged across the Zhongsha Trough, a failed rift
- The OCT features highly thinned continental crust with early stage magmatism and partially serpentinized upper mantle
- Continental breakup propagation controlled both the rifted basin reorientation and complexity of the crustal deformation

Supporting Information:

- Figure S1

Correspondence to:
X. Qiu,
xlqiu@scsio.ac.cn

Citation:
Huang, H., Klingelhoefer, F., Qiu, X., Li, Y., & Wang, P. (2021). Seismic imaging of an intracrustal deformation in the northwestern margin of the South China Sea: The role of a ductile layer in the crust. *Tectonics*, *40*, e2020TC006260. https://doi.org/10.1029/2020TC006260

Received 21 APR 2020
Accepted 22 DEC 2020

© 2021. American Geophysical Union. All Rights Reserved.

Seismic Imaging of an Intracrustal Deformation in the Northwestern Margin of the South China Sea: The Role of a Ductile Layer in the Crust

Haibo Huang[1,2], Frauke Klingelhoefer[3], Xuelin Qiu[1,2,4], Yuhan Li[1,4], and Ping Wang[1,2]

[1]Key Laboratory of Ocean and Marginal Sea Geology, South China Sea Institute of Oceanology, Innovation Academy of South China Sea Ecology and Environmental Engineering, Chinese Academy of Sciences, Guangzhou, China, [2]South Marine Science and Engineering Guangdong Laboratory (Guangzhou), Guangzhou, China, [3]Department of Marine Geosciences, IFREMER, Plouzané, France, [4]University of Chinese Academy of Sciences, Beijing, China

Abstract The continental margins of the South China Sea (SCS) have undergone episodic rifting since the Cenozoic, and there are ongoing debates surrounding the processes of crustal deformation and seafloor opening. In this work, we present a *P*-wave velocity model extending from the north of Xisha Trough to the Zhongshanan Basin in the northwestern SCS margin, using ocean bottom seismometer data of the wide-angle seismic profile OBS2013-1. The results show that the crust thins symmetrically across the western Xisha Trough, from more than ~20 km at the flanks to ~10 km in the central valley where the sedimentary layers thicken to over 6 km. In the Zhongsha Trough, closer to the deep basin, the upper crust is detached in a ~20 km wide region and the lower crust has seismic velocities increased by more than ~0.3 km/s. The top boundary of the lower crust is located at a depth of ~13 km across the Zhongsha Trough, and a ~5 km thick midcrustal ductile layer is imaged. A ~50 km wide ocean-continent transition region beneath the Zhongshanan Basin characterizes a ~6 km thick continental crust underlain by serpentinized and magnetized upper mantle. These observations, together with plate reconstructions based on gravity and magnetic analysis, suggest that deformation of the continental margin was controlled by a ductile crustal layer. Magmatism, associated with the early stage oceanic accretion, has mixed with the highly extended continental crust. Developments of the failed rifted basins were controlled by the westward propagation of the continental breakup.

1. Introduction

Rifting and lithosphere thinning eventually lead to continental breakup and oceanic spreading. As many continental margins show similar behavior in rifting, simple models were proposed to explain the crustal extension. For example, the "pure-shear" extension model was established to describe symmetric and uniform rifting (McKenzie, 1978), while the "simple-shear" model takes asymmetry further into account (Wernicke, 1981). Today, additional geophysical data challenge the abovementioned models and indicate a depth-dependent extension which favors strong decoupling between intracrustal layers (Hopper & Buck, 1996; Huismans & Beaumont, 2014; Lister et al., 1986). Depending on the lithologic composition, rheology and thermal structure of the continental lithosphere, passive margins can undergo progressive extension indicating variable styles of crustal deformation (e.g., Mohn et al., 2012; Peron-Pinvidic & Manatschal, 2019; Thybo & Nielsen, 2009).

The South China Sea (SCS) has been widely recognized as a Cenozoic marginal basin developed from atypical magma-poor passive rifting (e.g., Taylor & Hayes, 1983). In addition to extensive crustal stretching, the SCS margins also feature volcanic intrusion and a lower crustal high velocity layer (HVL) that are interpreted as magmatic underplating (Larsen et al., 2018; Yan et al., 2001). Over the years, geophysical surveys have revealed an asymmetrical conjugate pattern and the depth-dependent lithospheric extension of the margins in the SCS (Franke et al., 2014; H. B. Huang et al., 2019; Huismans & Beaumont, 2014). However, the rupture mode of the continental crust and the formation mechanism of the oceanic crust are still highly controversial. In 2017, the 367/368 International Ocean Discovery Program (IODP) drill legs were conducted in deep water (>3,000 m; Figure 1) at the edge of the northern margin of the SCS to reveal the nature of the structure from continent to ocean (Jian et al., 2018; Sun et al., 2018). The coring data suggest that the SCS has experienced fast lithospheric extension without mantle exhumation (Larsen et al., 2018), different from

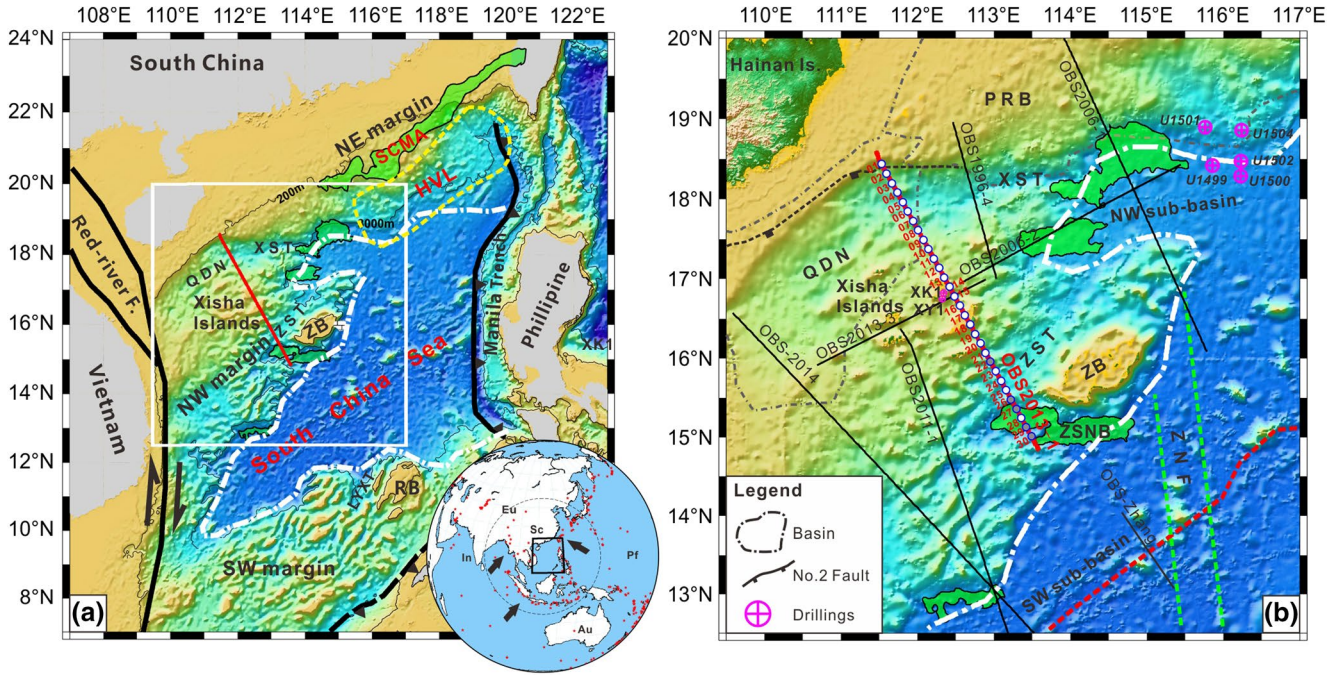

Figure 1. Location map showing the study region in the South China Sea. (a) High amplitude magnetic anomalies close to the slopes and in the northeastern (NE) margin are both represented by green masked polygons. Distribution of the HVL is enclosed by dashed yellow line. The dashed white line is the continent-ocean boundary (COB) referring to C. F. Li and Song (2012). The red line indicates the location of OBS2013-1. SCMA, South China Magnetic Anomalies along the NE margin of the SCS. RB, Reed Bank. The inset shows the tectonic setting of the SCS, in which, Eu is the Eurasia Plate, In is the India Plate, Au is the Australian Plate, Pf is the Philippine Plate, and Sc is the South China block. (b) Map showing the seismic profiles and the IODP drilling sites. OBS2013-1 is marked by a red line and the circles along the line represent OBS locations, in which, the white circles are OBSs recovered successfully while the gray ones are lost. Other profiles are labeled and shown as black lines, OBS2011-1 (H. B. Huang et al., 2019); OBS-2014 (Liang et al., 2019; Pichot et al., 2014); OBS1996-4 (X. L. Qiu et al., 2001); OBS2006-1 (Wu et al., 2011); OBS2006-2 (Ao et al., 2012; Wang et al., 2020); OBS2013-3 (Guo et al., 2016); and OBS-Zhang (J. Zhang et al., 2016a). The circles with cross are the IODP drillings. The dashed red line is the aborted spreading ridge. The Zhongnan Fracture Zone (ZNF) is outlined by the two dashed green lines, referring to C. F. Li and Song (2012). QDN, Qiongdongnan Basin; PRB, Pearl River Mouth Basin; XST, Xisha Trough; ZB, Zhongsha Bank; ZST, Zhongsha Trough; LYXT, Liyuexi Trough; ZSNB, Zhongshanan Basin.

the well-established margins along the Atlantic Ocean (Dean et al., 2000; Whitmarsh et al., 1993). In addition, early stage magmatism prior to steady-state seafloor accretion was detected overlying hyperthinned continental crust (~8 km thick) (Larsen et al., 2018). The seafloor accretion propagates from east to west, as revealed by interpretation of reflection seismic profiles (Franke et al., 2014). Accordingly, interlayer decoupling in the lithosphere could have been facilitated by the prerupture magmatism heating up and reducing the crustal viscosity (Franke et al., 2014).

The lithologic measurements of the sampled rocks should be closely combined with deep structure detection, such as geophysical exploration. The obtained seismic structures will provide an explanation for the rheological behavior of the continental crust (e.g., the weak zones and interlayer decoupling) that finally determines the pattern from rifting to breakup (Huismans & Beaumont, 2014). Moreover, original architecture and thermal structure of the crust usually evolved during poly-phased extension (Brune et al., 2014), and this requires comparison of deforming expressions in time and space. In this work, we present a *P*-wave velocity model from a wide-angle seismic survey spanning from the slope area in the northwestern margin of the SCS to the south of the Zhongsha Bank (Macclesfield Bank; Figure 1b). Seismic travel times were modeled to image the rift-related structures and to provide hints on the brittle/ductile behavior of the continental crust, and thus further insights into crustal deformation during rifting. The crusts show a regional deformation pattern in the failed rifts, and hyperthinned continental crust in the ocean-continent transition zone (OCT) is overprinted by early stage magmatism, which is in good agreement with the shallow lithology measurements from IODP drillings (Jian et al., 2018; Larsen et al., 2018; Sun et al., 2018).

2. Geological Setting

The SCS margins developed along a NE-strike divergent setting due to the rollback of the subducted Paleo-Pacific plate in the Late Mesozoic (Taylor & Hayes, 1983). Long-lasting continental rifting of the margins started in the latest Cretaceous to Early Paleocene (~65 Ma) and ceased prior to the progressive seafloor opening from ~32 to ~15 Ma (Briais et al., 1993; Larsen et al., 2018). As a result, the SCS evolved into segmented subbasins (Taylor & Hayes, 1983), and the margins also show along-strike deforming patterns of the continental crust (Franke et al., 2014; Hayes & Nissen, 2005). The eastern segment of the northern margin is characterized by the presence of an HVL (the location is shown in Figure 1a) underlying either hyperthinned continental crust or separated upper crust (McIntosh et al., 2014). A remarkable high magnetic anomaly belt in the northern margin (SCMA) has long been discussed and is considered a remnant of a Mesozoic subduction arc (Wan et al., 2017). In comparison, the western section exhibits a normally extended continental crust (Hayes & Nissen, 2005), alternating with aborted rifts and rigid blocks over a broad region. However, volcanic relics associated with the Mesozoic subduction have also been recognized along the northwestern and conjugate margins, characterized by sporadically distributed high-amplitude positive magnetic anomalies (F. C. Li et al., 2018). Whether the HVL exists in these areas is debated, as several wide-angle seismic surveys reported its absence (X. L. Qiu et al., 2001; Wu et al., 2011), whereas a few reflection seismic surveys and gravity modeling revealed scattered HVLs (Pichot et al., 2014; N. Qiu et al., 2013). Besides, in terms of the amount of stretching within the crust (J. J. Zhu et al., 2016), the performance of the ductile crustal layers also shows strong discrepancy between different investigations.

The NW margin of the SCS bounded by the Red River Fault Zone in the west (Figure 1a) retains lithospheric deformation features from episodic rifting. Basin analysis has revealed a zonal distribution of tectonic stresses (Ren & Lei, 2011), including the collision-induced extrusion of the Indochina block in the west that has formed pull-apart basins such as the Yingehai Basin, Zhongjiannan Basin, and the eastern Qiongdongnan Basin (Figure 1b). For the eastern part, where the Xisha Islands (Paracel Islands) and the Zhongsha Trough are located, grabens and horsts were mainly shaped by normal and low-angle faults in extension and characterized by ductile shearing of the continental crust (Lei & Ren, 2016). Wide-angle seismic surveys have imaged highly extended continental crust with a thickness of less than 8 km along these troughs and basins, for example, the Xisha Trough, which represents an aborted rift (X. L. Qiu et al., 2001). Seismic surveys using seafloor cables have identified strong postspreading volcanism and hydrothermal activity along the rift faults, while the syn-rift igneous rocks are sporadically distributed (Zhang et al., 2016b).

Tectonic subsidence is considerably delayed for more than 10 Myr due to ongoing rifting or rising asthenospheric material along the NW margin (Franke et al., 2014), and the uplifted basement thus provided a prosperous position for the growth of reefs around the Xisha Islands (Ma et al., 2011). Controversy still exists mainly around the basement nature and age beneath the islands. Several boreholes have been drilled on the islands for dating and classifying the basement rocks (e.g., XY1 and XK1 in Figure 1b). Precambrian granitic rocks were drilled and dated at borehole XY1 (M. S. Zhang, 1991). Nevertheless, results from the latest coring data from borehole XK1 indicate that the basement rocks are constituted of Late Mesozoic igneous rocks, possibly representing the widespread volcanic intrusions over the SCS due to the Paleo-Pacific subduction (W. L. Zhu et al., 2017). Volcanic rocks dredged near Zhongsha Bank in the east of the Xisha Islands were also dated to the Late Mesozoic (Jin, 1989). Geophysical surveys show that the Zhongsha Bank consists of extended continental crust with a thickness of more than ~20 km (Wu et al., 2011). Localized crustal deformation and magmatism were prevailing at the edge of these continental banks, as indicated by reflection seismic surveys and analog modeling on the stretching mechanism of the rigid blocks (Ding & Li, 2016).

3. Data and Methods

3.1. Data Acquisition and Seismic Phases

In April and May 2013, the "Shiptime Sharing Project of NSFC" conducted a geophysical cruise across the Xisha Islands using the R/V "Shiyan 2." During the cruise, a ~500 km long wide-angle seismic profile (OBS2013-1; Figure 1b) striking NW-SE was acquired spanning from west of the Xisha Trough to the south of Zhongsha Bank and coinciding with a multichannel reflection seismic profile of four stream-

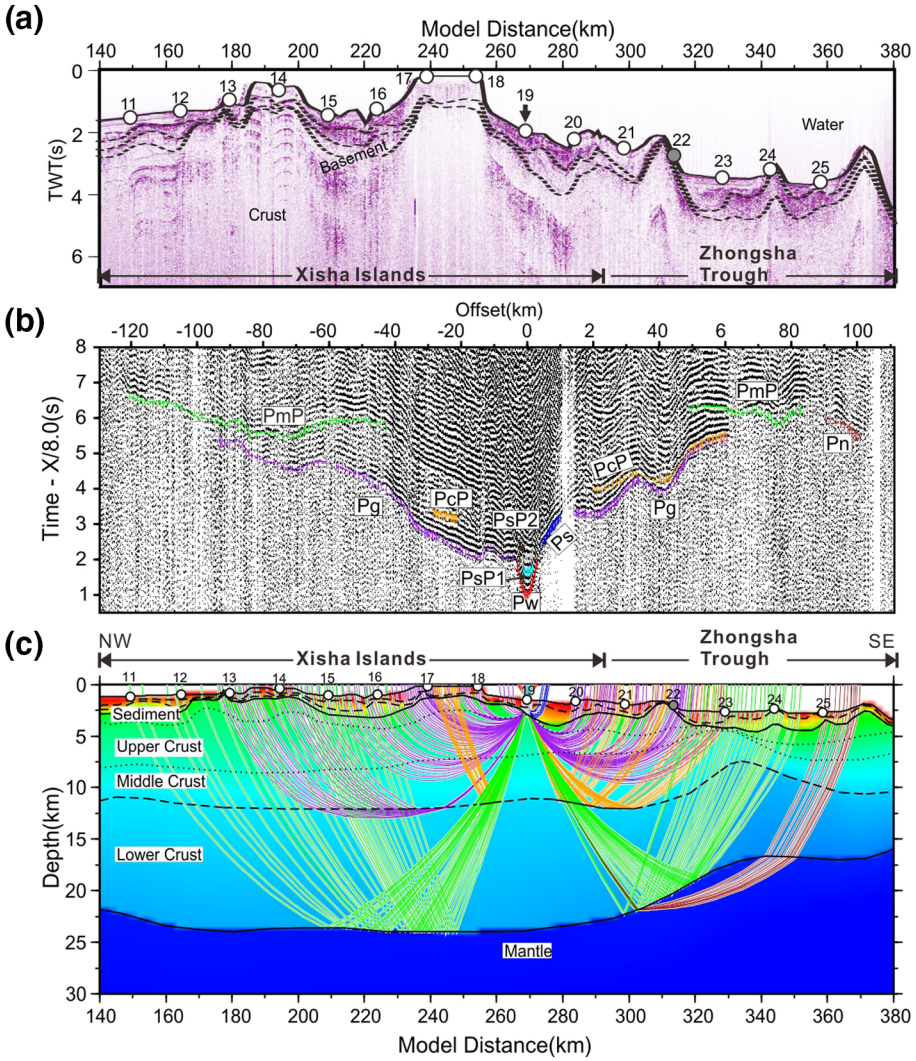

Figure 2. Seismic modeling of the OBS data. (a) A segment of the reflection seismic data section. The white circles mark locations of the recovered OBSs, while the gray ones mark those who are lost. The solid line and the dashed lines respectively represent the seafloor and the sedimentary interfaces from the forward modeling. (b) Seismic section of OBS19, overlain by the calculated travel times in different colors. The reduction velocity is 8.0 km/s. Location of OBS19 is shown in Figure 1b. (c) A segment of the forward velocity model. Seismic ray paths are shown by colored lines.

ers. Thirty ocean bottom seismometers (OBS) spaced at ~15 km were deployed, among which 25 OBS were successfully recovered and provided useful data. Four air guns with a total volume of ~98 L were deployed ~30 m behind the vessel and shot every 120 s, leading to ~300 m shot spacing at a ship speed of ~5.0 Kn.

The raw seismic data were corrected for the clock-drift, and instrument positions were relocated by fitting the direct water-wave traveltimes using the least-square method (West et al., 2001). A spectrum-whitening deconvolution was used to remove the bubble reverberations and highlight the primary arrivals. Automatic gain of the seismic amplitudes and zero-phase band-pass filter (3–15 Hz) were also applied to further enhance the seismic signals. The reflection seismic data were processed following basic steps, including trace sorting, filtering, and automatic gain. The OBS sections show clear refracted phases traveling though the sediments (Ps), the crust (Pg), and the upper mantle (Pn). Sedimentary reflections (PsP1 and PsP2) as well as reflections from top basement (PsP3), mid-crustal interface (PcP) and the Moho (PmP) were also identified (Figures 2–4). A total of 10,346 arrivals including 5,856 refractions and 3,992 reflections were finally

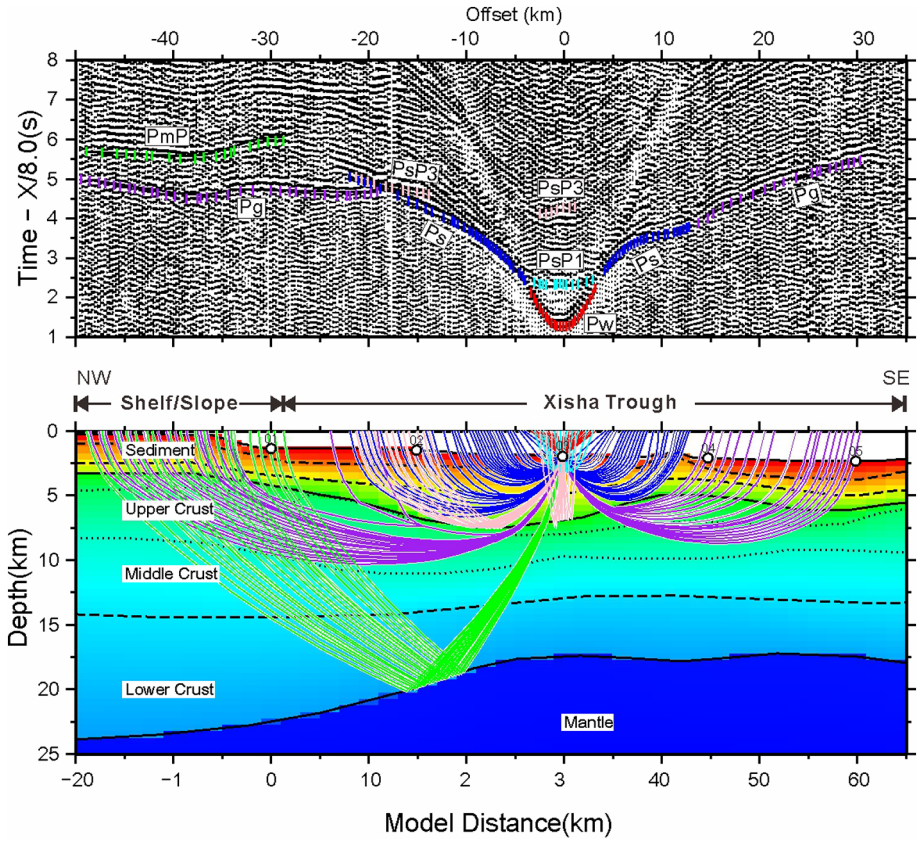

Figure 3. Seismic modeling of the data from OBS03. The reduction velocity is 8.0 km/s. Location of OBS03 is shown in Figure 1b. Seismic ray paths are shown by colored lines.

picked. Picking uncertainties were assigned to the phases ranging in 50–70 ms, based on the signal-to-noise ratio.

3.2. Velocity Modeling

The *P*-wave velocity structures were jointly constrained by forward modeling (Zelt & Smith, 1992) and tomographic inversion (Korenaga et al., 2000) of the seismic traveltimes. A combination of both approaches allows to conclude a user-independent velocity model including as much available information as possible (H. B. Huang et al., 2019). The forward modeling was performed using the layer-stripping method to decrease the misfits between the picked and calculated traveltimes (see Figures 3 and 4 and the supporting information). First, a three-layer sedimentary model with variable velocities in a range of 1.7–4.5 km/s below the seafloor was constructed by forward modeling of the Ps and PsP phases. Velocities within the sediments influence the seismic phase morphologies, which is more easily identified when the sedimentary layer is less undulating, as imaged in the left branch of Figure 3. Velocity boundaries between the sedimentary layers as well as the basement were converted from depth to two-way traveltime and match the reflection seismic data well (Figure 2a). Second, tomographic inversion of the crustal structures was implemented using Pg and PmP phases, taking the sediments as input information. Finally, the inversion model was further revised by forward modeling to prevent over interpretation of small-scale anomalies of the velocity and the Moho. In addition, the forward modeling allows imaging of intracrustal structures by fitting the secondary arrivals (Liang et al., 2019). Velocity boundaries within the crust were continuously traced by the PcP phases (Figure 4), thus providing information for imaging the layered structures of the crust (Figure 2). The identification and modeling of the intercrustal interface were verified by calculating the synthetic waveforms based on zero-order asymptotic ray theory (Zelt & Ellis, 1988). Basically, the theoretical PcP phases

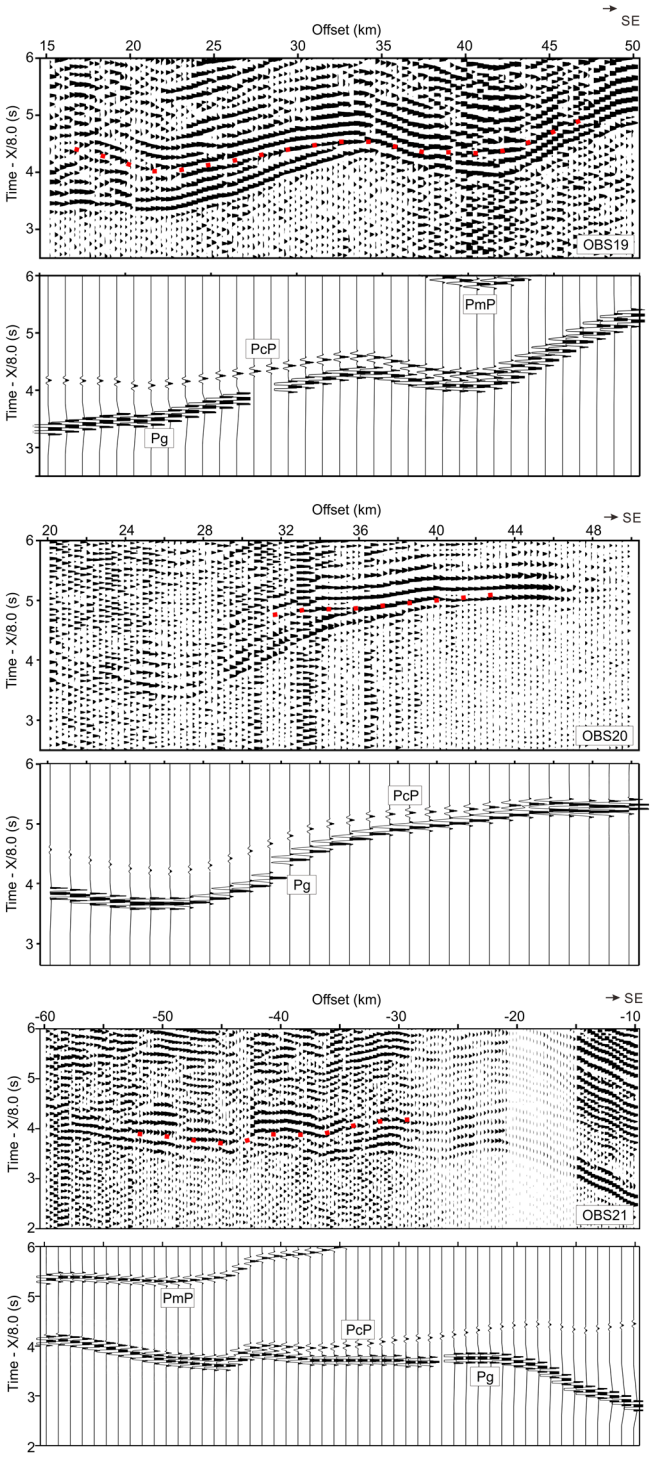

Figure 4. The PcP phases recorded in OBS19, OBS20, and OBS21. Red dotted lines denote the picked PcP phases. For each OBS, the upper panel shows the real seismic profile, while the lower panel shows the synthetic one based on the velocity model and the calculated traveltimes. The reduced velocity is 8.0 km/s.

with relatively higher amplitudes correspond to the real phases that are easy to pick (Figure 4). The velocities of the upper mantle were modeled based on the Pn phases once the crust was well constrained.

4. Results

Modeling of the OBS2013-1 data resulted in a velocity model showing sedimentary and crustal structures along the complete NW margin to a depth of 30 km (Figure 5b). As they show more intracrustal detail constrained by the secondary phases, the sedimentary and crustal structures of the forward model will be discussed with the interpretation of the reflection seismic data. This helps to better understand the deforming pattern of the continental crust as well as the magmatic activity along the margin. The modeling errors are discussed below, and main features of the velocity model are described according to the major tectonic units.

4.1. Error Calculations of the Velocity Model

The tomographic model shown in Figure S1a was parameterized in a grid mesh with node spacing of 0.5 km in the horizontal dimension and 0.05–0.25 km in the vertical dimension increasing downward. The Moho and the intercrustal boundary were both defined with uniform 1 km spacing. Smoothing weighting factors for the velocity and depth were set to 200 and 20 after conducting a set of trials to avoid artifacts in the velocity models. Checkerboard tests of the model resolution were applied to perturbed models with the same mesh as the final tomographic model (Figure S2) (Korenaga et al., 2000). The synthetic traveltimes were calculated using the same shot-receiver geometry as the real data. A rectangular perturbation pattern of 8% of the velocities, with a horizontal cell-size of 25 km and vertical cell-size 6 km can be successfully recovered (Figures S2b and S2c). There is little difference between the tomographic and the forward models in most areas (Figure S1b), except for some small-scale high amplitudes observed beneath the sharp basement highs. However, the velocity perturbation and sizes in both models are within the identifiable range as indicated by the checkerboard tests.

The RMS error (root-mean-square value) and χ^2 (chi-squared value) of the misfits, which evaluate robustness of the forward model, are respectively 0.067 and 1.383 using 95.3% of the picked traveltimes. The uncertainty of the layered structures in the final forward model was assessed using a Monte Carlo approach (VMONTECARLO; Loureiro et al., 2016). To prove the uniqueness of the final model and estimate the uncertainty of the varied depth and velocity nodes, this method generates and runs a large number of randomly perturbed models in given bounds. A scoring function is built from the results of each run based on the χ^2 value, and a subset of models within user-defined thresholds is used to calculate model uncertainties. In this study, 500,000 randomly varied models were produced from the final forward model, and used to produce an uncertainty map of all velocity and depth nodes (Figure 6). Generally, the velocity uncertainty varies between ±0.3 km/s while the Moho-depth uncertainty ranges between ±1 km, so the model is well resolved in nearly all regions. The largest velocity uncertainty values are located near the Moho and the intercrustal interface. However, this may be due to a strong trade-off

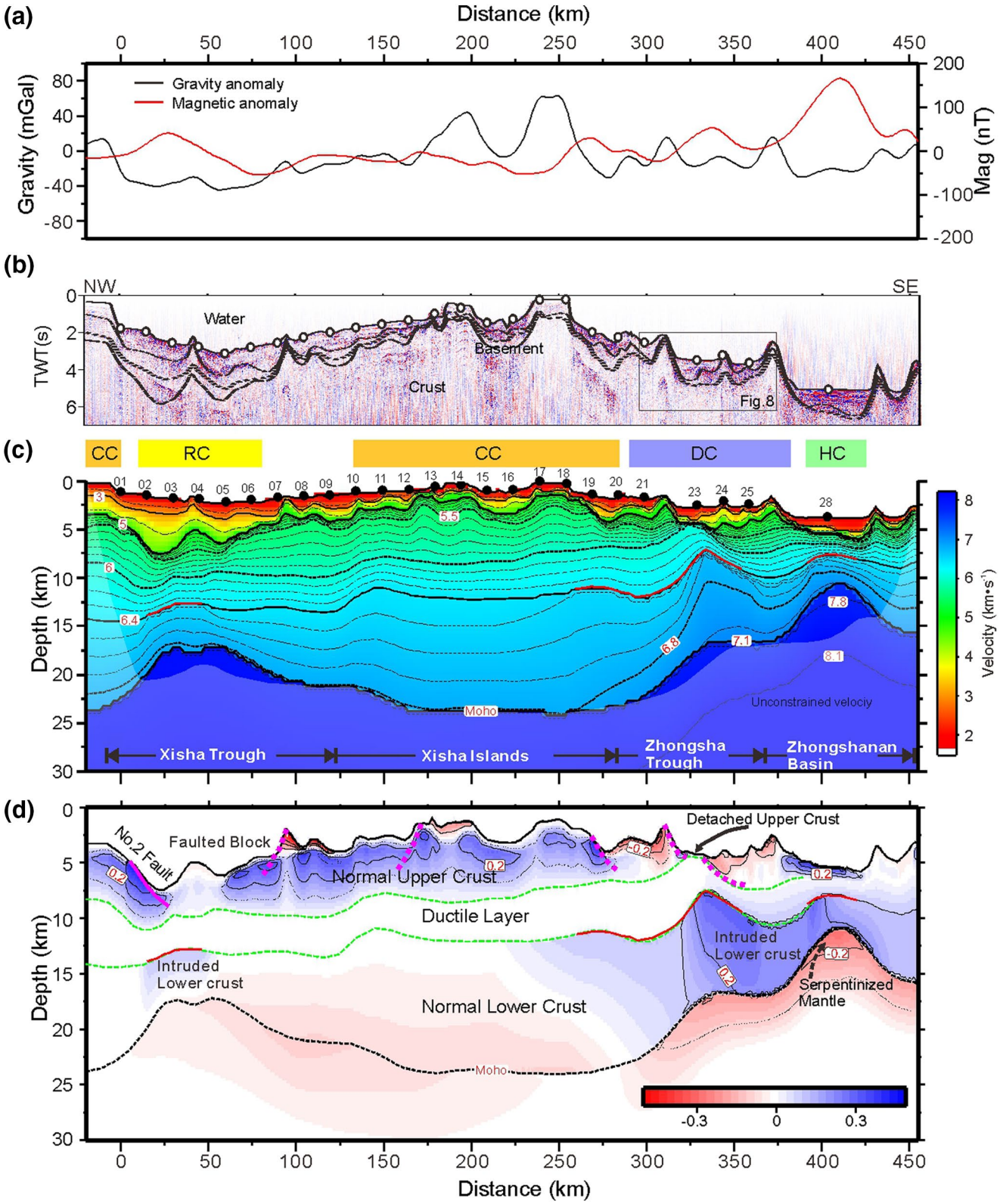

Figure 5. Final forward model and velocity perturbation of the OBS2013-1. (a) Gravity anomaly (black line) and magnetic anomaly (red line). (b) Reflection seismic data section. The box is shown in Figure 8. (c) *P*-wave velocity model. CC, continental crust; RC, rift valley crust; DC, detached crust; HC, hyperthinned crust. (d) Velocity perturbation in the crust, with respect to the horizontal mean value of the forward model, shown in positive (blue) and negative (red) values. The thick red lines show the faults cutting the basement. The green lines outline the ductile layer between the normal upper crust and the lower crust. The black dashed line shows the Moho, while the thin red solid lines show the constraint intercrustal interface.

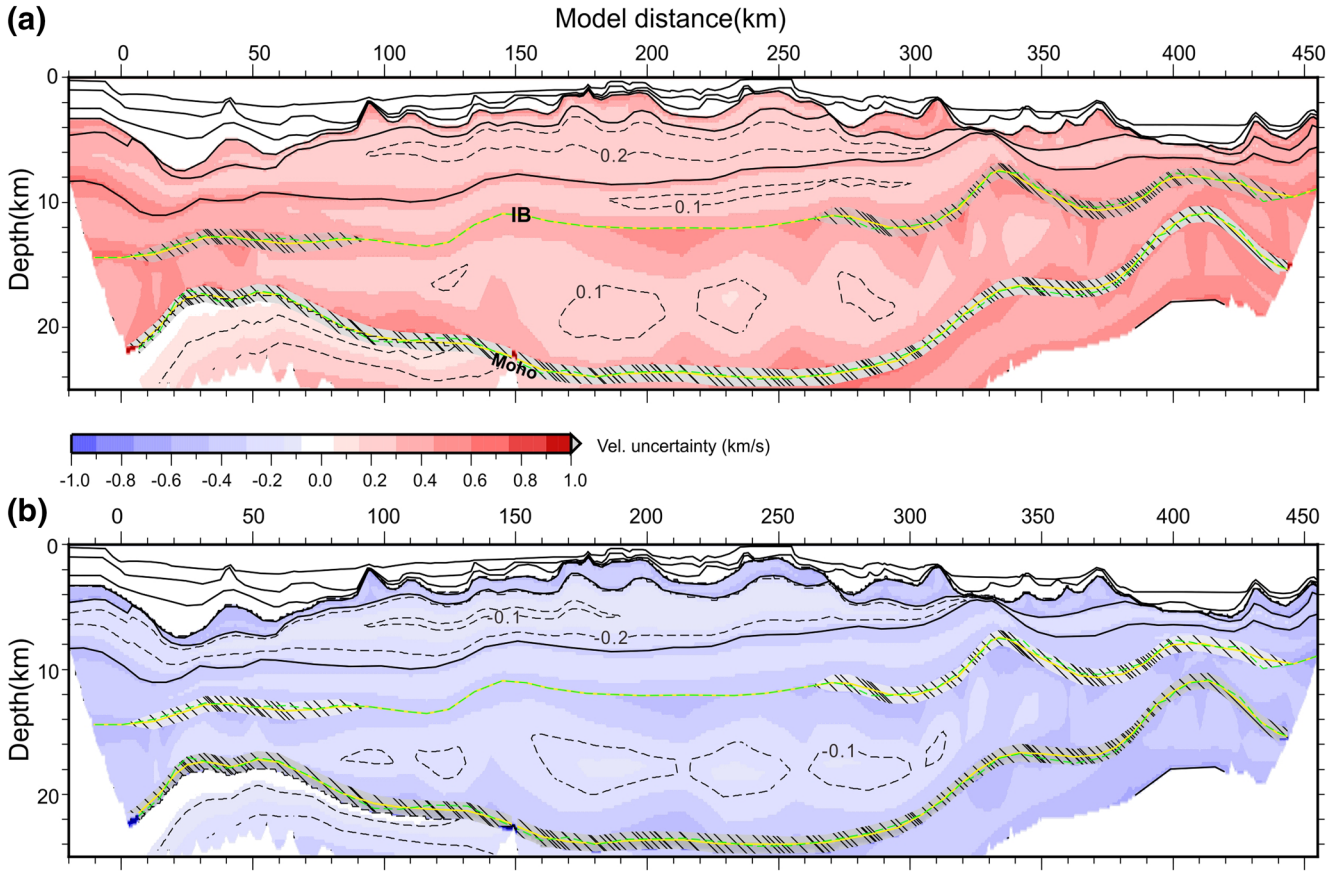

Figure 6. Monte Carlo uncertainty tests of the forward model. The hatched areas at the intracrustal boundary (IB) and the Moho denoted the depth uncertainties for both the boundaries. Dashed yellow and green lines, respectively, indicate the best random model and the forward model's IB and Moho. (a) Maximum and (b) minimum admissible velocity deviations from the forward model.

between depth and velocity at the velocity boundary but does not reflect the model quality (Loureiro et al., 2016).

4.2. Velocity Structure Beneath the Xisha Trough and Its Flanks

A 3- to 6-km-thick Cenozoic sedimentary sequence was imaged along the west Xisha Trough, composed of three layers with velocities of 1.7–4.5 km/s and velocity discontinuities between 0.1 and 0.5 km/s across the interfaces. The top of the basement is characterized by a long-wavelength morphology variation across the section, showing a progressive deepening toward the shelf foot. This results in a thickened sedimentary layer and the formation of a ~70 km wide half-graben. A basement high is located at the trough center and overlain by a seamount with average seismic velocity of ~3.5 km/s. For comparison, the sedimentary cover of the Xisha Islands is much thinner (~2.5 km) and overlies a relatively shallow basement at ~3 km depth (Figure 5c).

The Moho is located deeper than 22 km below the shelf at Xisha Islands, and rises progressively toward the Xisha Trough to ~17.5 km. The *P*-wave velocity increases from 5.0 km/s at the basement top to ~6.8 km/s at the bottom of the crust. A ~0.1 km/s velocity contrast boundary near the isovelocity contour of 6.4 km/s was sampled by the PcP phases in a 30-km wide area.

4.3. Zhongsha Trough and Zhongshanan Basin

A series of horsts and grabens developed across the Zhongsha Trough, with basement highs and intermediately thick sedimentary deposits (~3 km). Velocities at the basement top vary between 5.0 and 5.6 km/s.

The Moho becomes shallower rapidly from ~23 km in the Xisha Islands to ~15 and ~11 km respectively in the Zhongsha Trough and the Zhongshanan Basin, over a distance of ~100 km. The crustal thickness is ~6 km in the Zhongshanan Basin, where a lens-shaped layer less than 2 km thick was modeled by seismic velocities of ~3.8 km/s on top of the basement. This was also identified in the reflection seismic section and corresponds to a high positive magnetic anomaly (~170 nT; Figure 5a).

The crustal velocities also show a complex variation across the Zhongsha Trough. The upper crust, taking the 6.4 km/s isovelocity line as the lower boundary (Christensen & Mooney, 1995; Rudnick & Fountain, 1995), is stretched to become less than 5 km thick and accompanied by uplifted lower crust. To provide a more intuitive view of the crustal structures, the velocity variation of the forward model is calculated within each crustal layer, with respect to the average value at a constant depth below the interface (Figure 5d). Accordingly, velocity in the lower crust increases by ~0.3 km/s from the mean value forming a sharp velocity contrast across the boundary (Figures 5c and 5d), which can be continuously traced in a range of ~90 km by the PcP phases (Figure 4). A similar intercrustal velocity boundary is located beneath the Zhongshanan Basin, where the velocity contrast is slightly reduced to 0.1–0.2 km/s (Figures 5c and 5d). The uppermost mantle beneath the basin shows an average velocity of ~7.7 km/s, lower than in adjacent areas, in a horizontal range of ~50 km and vertical depth of more than 3 km from the Moho, which is constrained by the Pn phases in OBS25 and OBS28 (Figures S24 and S25).

5. Discussion

5.1. Intracrustal Deformation and Identification of a Ductile Layer

The detailed mapping of the intercrustal boundary and the Moho in the velocity model provides direct evidence of intracrustal deformation. The model can be divided into four distinct sections according to the crustal structures in Figure 5c. The Xisha Islands and the shelf area in the northern Xisha Trough are identified as continental blocks that have experienced weak and uniform stretching. The crustal thickness (~22 km) is in good agreement with the values derived from the receiver functions on the islands (H. B. Huang et al., 2011). Along the western Xisha Trough, the crust has been stretched to be as thin as ~10 km beneath the half graben called Songnan Sag of the Qiongdongnan Basin (Lei & Ren, 2016). Between OBS01 and OBS02, the top basement shows an velocity increased by ~0.5 km/s compared to both sides (Figure 5d), which is also proposed by N. Qiu et al. (2013). In earlier work, it was proposed to represent a detachment fault that shaped the half graben within the basin (Lei & Ren, 2016). This fault may not only contribute to the gravity anomaly identified along our model (Figure 5a), but also the associated variation of the seismic velocity (Figure 5d). A similar complex basement shape was also presented by X. L. Qiu et al. (2001), and the basement high in the center can be interpreted as a rotated continental block related to a rollover anticline (Lei & Ren, 2016). Using an initial crustal thickness of 30 km, it corresponds to a stretching factor β of 3.0 that is lower than the value calculated for the Xisha Trough (β = ~3.8; X. L. Qiu et al., 2001), due to a higher degree of crustal thinning in proximity to the oceanic basin.

Along the southern part of the profile, a prominent rise of the Moho and a relatively shallower basement than in the north are modeled, reflecting the delayed subsidence of the NW margin of the SCS (Franke et al., 2014). Instead of a wide rift valley like the Xisha Trough, a series of half grabens distributed along this region bordered by seaward dipping faults and corresponding basement highs were imaged. These faults extend down to depths of ~7 km where the velocity shows high perturbations and distinctive gradients (Figures 5c and 5d). Strikingly, the crust with velocities lower than 6.0 km/s is dismantled along a small window about 20 km wide in the Zhongsha Trough (near OBS23), with rotated basement on both flanks that might also represent rollover structures. Such crustal structures show strong similarities on several wide-angle seismic profiles (Figure 7), including OBS2011-1 in the southwest extension of the Zhongsha Trough (H. B. Huang et al., 2019) and OBS2014s in the Liyuexi Trough (Basin C in Liang et al., 2019). In all profiles, the seaward dipping detachment faults are recognized along the basement highs, beneath which the crust is stretched to be ~10 km and the crust above 6.0 km/s is highly stretched or dismantled. The large-scale detachment fault, featuring exhumed middle/lower crust and extension-

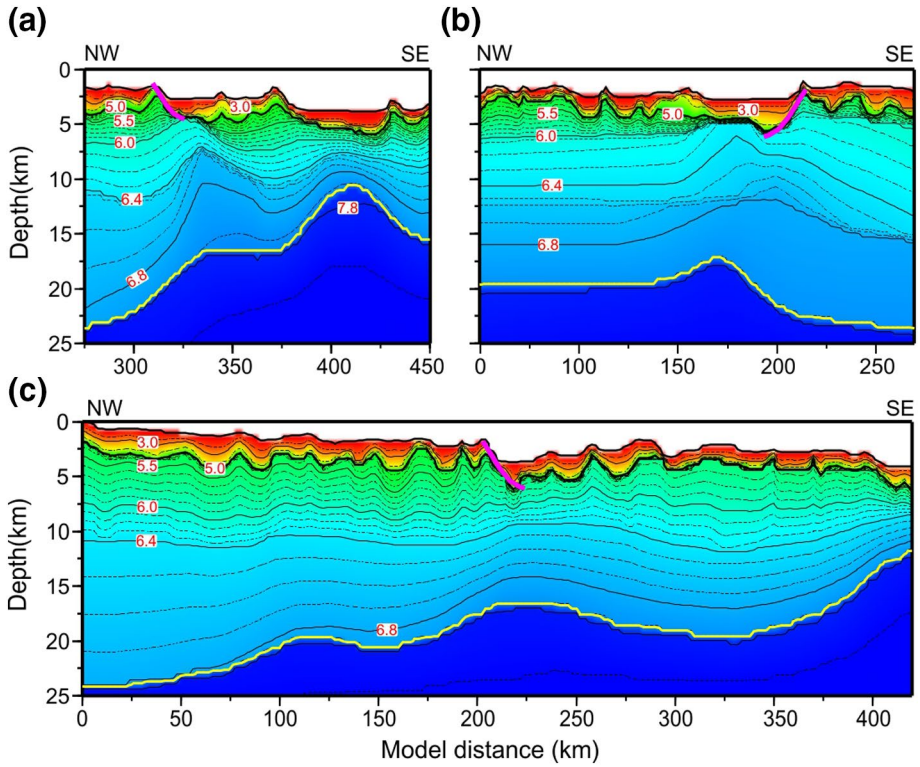

Figure 7. Comparison of the forward velocity models on the margins of the SW subbasin. (a) The model of OBS2013-1 in this study. (b) The model of OBS2014s (Liang et al., 2019). (c) The model of OBS2011-1 (H. B. Huang et al., 2019). The purple lines mark the identified detachment faults, and the yellow lines mark the Moho interfaces. Location of the profiles is shown in Figure 9a.

al-parallel corrugation, has also been documented in the northern SCS margin (Liwan detachment fault, in Deng et al., 2020). The rift parallel structures may also be shown in the enlarged topography map of the Zhongsha Trough (Figure 8), where two parallel ridges of ~30 km in length are separated by ~12 km. If this is supposed as the corrugation structures, the aspect ratio of ~2.5 is highly consistent with the value of the Liwan detachment fault (Deng et al., 2020). However, the nature and origin of these ridges still remain unclear, as the seismic profile obliquely crosses the structures and high-resolution seismic surveys are lacking for this zone.

The top boundary of the lower crust can be imaged in an extended range, buried at a depth of ~13 km across the Zhongsha Trough (Figure 5c). Previous long streamer seismic surveys also imaged reflectors at around ~15 km depth in the northern and western SCS margins, where listric faults extend and may represent the brittle-ductile transition zone (Lester et al., 2014). By considering the brittle deformed upper crust along the detachment fault, we propose that a ~5 km thick ductile layer exists beneath the upper crust, separated from the lower crust by a shearing surface (Figures 5c and 5d). Reflected phases from the top boundary of this ductile layer were not detected, possibly due to a small seismic impedance contrast or a low resolution of the OBS data. The lower crustal thickness beneath the shearing surface appears to be 2–3 km higher under the Zhongsha Trough than the blocks on both sides (Figure 5c). The bottom of the lower crust shows slightly increased velocities of up to 7.1 km/s (Figure 5c and 5d). Nevertheless, the average lower crustal velocity of ~6.8 km/s is much lower than the HVL in the NE margin that characterizes volcanic underplating (Wan et al., 2017), reflecting different extents or sources of volcanic activity. Instead, this may indicate magmatic additions compensating the expected Moho uplift during rifting, similar to the Kenya and Baikal rifts (Thybo & Nielsen, 2009). From our model, the highly reflective top of the lower crust indicates a prominent velocity/density contrast, which could have been enhanced by a front of intruded sills blocked at the ductile boundary (Figures 5d, and 10c, and 10d). Previous studies suggest that a weak middle crustal layer is important for compensating the upper crustal extension, while

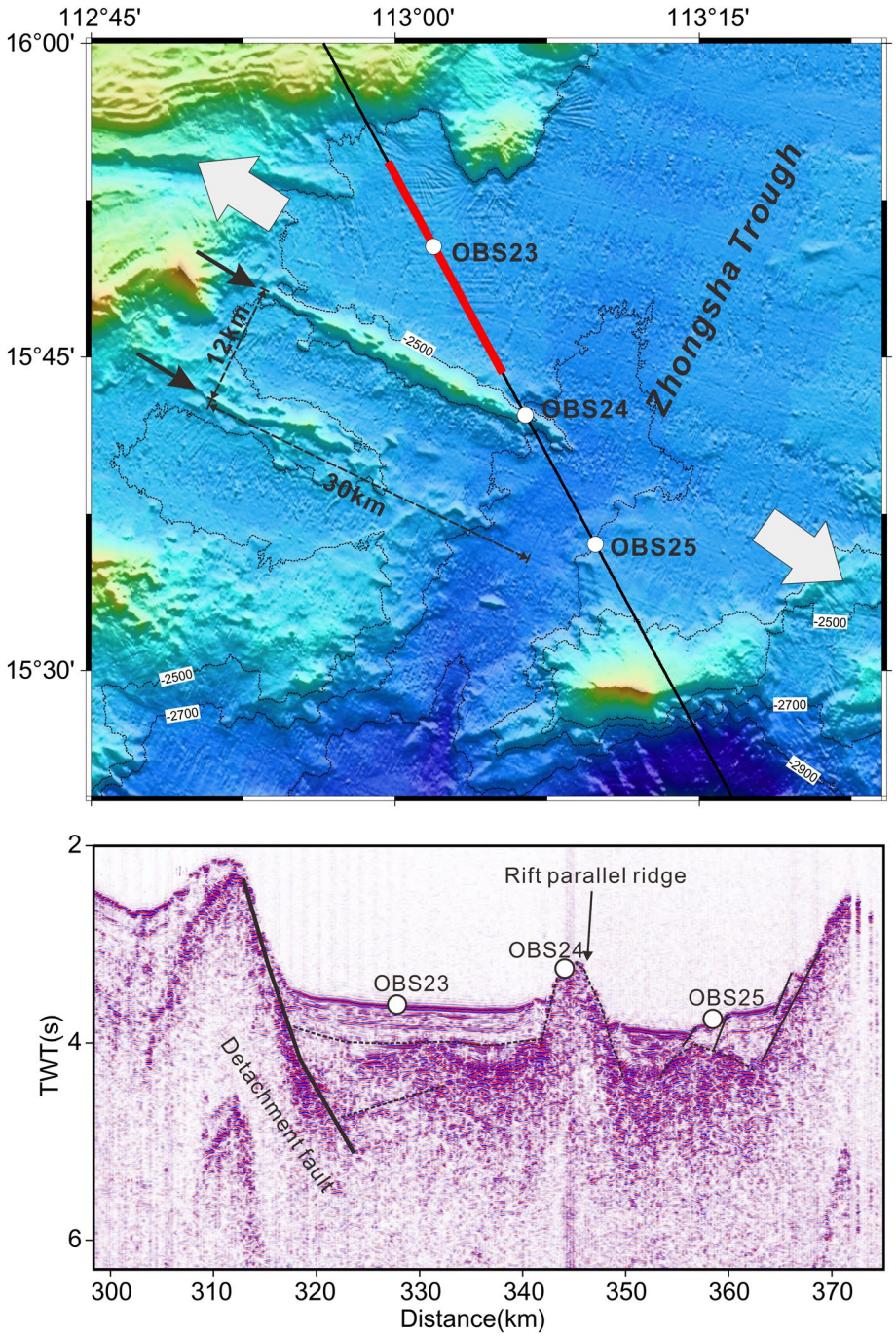

Figure 8. Zoom on the topography of the Zhongsha Trough (top), where the white circles are OBSs and the two solid arrows show the rift parallel ridges. The white arrows indicate the rifting direction of the Zhongsha Trough. The lengths and crest-to-crest wavelength of the ridges are 30 and 12 km, respectively. The red line indicates the place where dismantled upper crust is observed. Reflection seismic image of the ridges (bottom).

the lower crust is likely to be strong in the NW margin of the SCS (Franke et al., 2014; F. C. Li et al., 2019). This could be partly supported by the increased velocity due to intrusion and strong thickness variation of the lower crust (Franke et al., 2014). However, the ductile/brittle nature of the lower crust can evolve through time as thermal conditions change (Mohn et al., 2012; Savva et al., 2014), and the entire lower crust can become ductile and flow (e.g., in Liang et al., 2019).

5.2. Hyperthinned Continental Crust in the OCT

A stretching factor of ~5 can be calculated in the Zhongshanan Basin off Zhongsha Bank, representing a possible location for breakup of the continental crust (R. White & McKenzie, 1989). To determine the nature of the crust, averaged velocity-depth profiles were extracted from the velocity model (Figure 9b). The results show that the crustal velocities and thickness are in good agreement with those from typical Atlantic oceanic crust (R. S. White et al., 1992). A two-layer structure, separated by a clear velocity step, represents the oceanic Layers 2 and 3. However, the magnetic anomaly in this area does not show the pattern with clear stripes as found in the deep basin representing the steadily formed oceanic crust (Figure 9a). Such long-wavelength magnetic anomalies can also be identified alongside other slope regions of the SCS (Figure 9a). Here, the buried layer (velocity of 3.8 km/s) overlying the basement may represent volcanic extrusions and contribute partly to the magnetic anomaly. In addition, the horizontally overlying strata indicate that these magmatic activities occurred earlier (Figure 9c). A similar magnetic anomaly has been observed along the Central and North Atlantic margins, representing prespreading magmatic intrusions or underplating (Nirrengarten et al., 2017). The anomaly also occurs over a basement with a velocity structure characteristic of oceanic crust, but its nature and origin are questioned. Instead, normal crustal velocities (5.0–7.0 km/s) and a reflective Moho in our model exclude both underplated material from mantle melting and exhumed mantle as an explanation for these anomalies. More likely, the faults at the rim of the blocks, as well as the igneous intrusions suggest the presence of a hyperthinned continental crust in this region.

We also compiled the crustal structures along the slope regions with strong magnetic anomalies in the NW margin and the oceanic basins from published velocity models (Figure 9b) (H. B. Huang et al., 2019; Wu et al., 2011; Zhang et al., 2016a; Zhao et al., 2018). The structures share common characteristics including a narrow high velocity band and a high velocity gradient of the upper crust similar to the global characteristics of the OCT (Christensen & Mooney, 1995). Variation of crustal thicknesses (6–9 km) can be explained by extents of magmatic additions or influences from prerifting structures. In contrast, the normal oceanic crust is relatively thin, around 5–8 km. The seismic velocity and gradient of Layer 2 in the spreading ridge (C5e-C5c) decreased rapidly compared to near the OCT region (C12-C11) (Figure 9b), reflecting a greater degree of fracturing and less compaction of the cracks (R. S. White et al., 1992). At the same time, there are similar velocity differences between the OCT and the oldest oceanic crust compiled from the NW subbasin (Figures 9a and 9b). The narrow OCT (~50 km) and the prominent magmatism suggest that the early stage oceanic crust may have merged into the highly fractured continental crust. The results are consistent with the IODP drilling that revealed a narrow and fast rift-to-drift transition with abundant MORB-type melts along the margin of the NW subbasin (Larsen et al., 2018).

5.3. Origin of the Low-Velocity Upper Mantle and the High Magnetic Anomaly

The obvious low-velocity structure (~7.7 km/s; Figures 5b and 5c) extending more than 3 km below the Moho in the Zhongjiannan Basin can be interpreted as an indicator of serpentinization in the upper mantle (Miller & Christensen, 1997) or the presence of partial melting (Henry et al., 1990). The ~3 km thick molten material with velocity of ~7.7 km/s would have required a Moho temperature higher than 1000°C (White & McKenzie, 1989). However, the heat flow value measured here is about 60 mW/m^2 (Shi et al., 2002), which indicates that the temperature below the crust is less than 500°C, not high enough to cause extensive melting. The long-lasting rifting and crustal cooling likely lead to a completely brittle crust and faults cutting into the upper mantle (Franke et al., 2014; Perez-Gussinye & Reston, 2001). In addition, as the regional extension was accommodated by intrusion, the detachment system will be replaced by high angle normal faults as the strain rate decreases (Bosworth, 1994). Since the crust is only ~6 km thick, serpentinization could originate from penetration of water into the upper mantle through the normal faults bordering the blocks (Figure 10c) (Dean et al., 2000). In this scenario, seismic velocity of ~7.7 km/s corresponds to about 13% of the partial serpentinization of the upper mantle (Mechie et al., 1994). Similar serpentinized upper mantle has been proposed to exist beneath the fossil spreading ridge in the SW subbasin, where very thin oceanic crusts and widely distributed crustal faults were measured (Yu et al., 2018; Zhang et al., 2016a). Nevertheless, the limited extent and

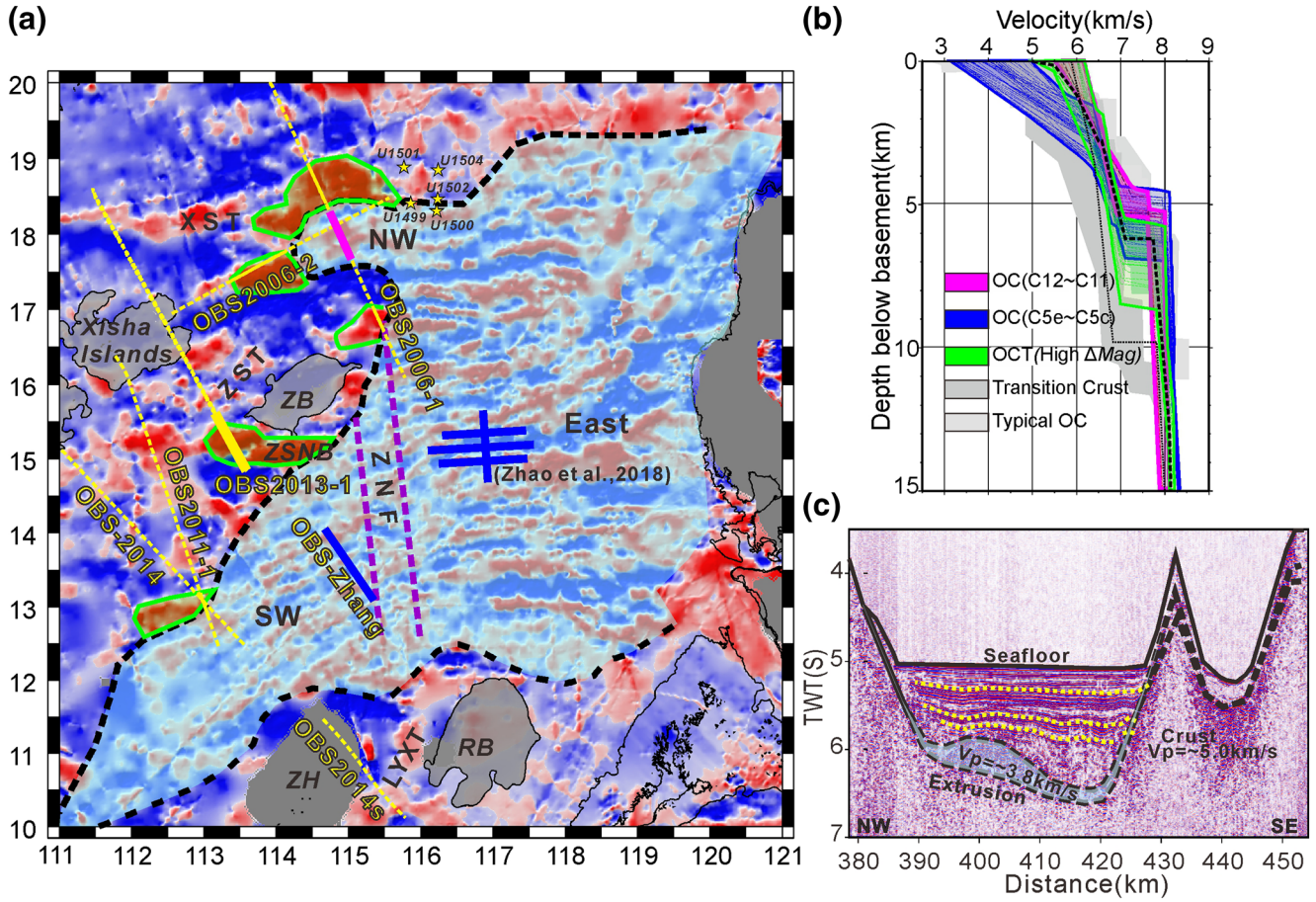

Figure 9. (a) Magnetic anomaly map of the SCS. Dashed yellow lines denote OBS profiles along the NW margin, while solid blue lines denote the ones at the spreading ridge. The solid purple line denotes a segment of the OBS2006-1 in the NW Subbasin. Green lines enclose high magnetic anomalies near the slopes. Yellow stars are IODP drillings during the 367/368 cruises. NW, Northwestern Subbasin; East, Eastern Subbasin; SW, Southwestern Subbasin; RB, Reed Bank; XST, Xisha Trough; ZB, Zhongsha Bank; ZST, Zhongsha Trough; LYXT: Liyuexi Trough; ZH, Zhenghe Massif; ZNF, Zhongnan Fracture Zone; ZSNB, Zhongshanan Basin. (b) Compilation of the velocity structures in the SCS. The dashed line represents the averaged velocity-depth profile in the Zhongshanan basin. OC, Oceanic crust. (c) A segment of the reflection seismic profile along the OBS2013-1, which is denoted by the bold solid yellow line in Figure 9a. The yellow dotted lines denote the sedimentary boundaries, and the transparent shaded area denotes the buried volcanic extrusions.

degree of the serpentinized mantle may indicate short-term fault activity (Bayrakci et al., 2016) or high temperatures at that time (Perez-Gussinye & Reston, 2001). This again agrees with the narrow OCT in the study region due to the rapid onset of oceanic crust accretion.

Spectral analysis of the magnetic field in the SCS indicates that deep magnetic layers at the lower crust or upper mantle contribute to both the SCMA and anomalies near the OCT (C. F. Li & Song, 2012). The mantle serpentinization of ~13% beneath the Zhongshanan Basin, if it exists, is likely not be the dominant source of the high magnetic anomaly in this area, as very partially serpentinized upper mantle makes a limited contribution to the magnetic anomaly (Fujii et al., 2016). The long-wavelength magnetic anomalies were frequently observed over cratons and forearcs and were considered to be caused by magnetic uppermost mantle (Ferre et al., 2014). Forward modeling of the magnetic anomalies from xenoliths shows that high magnetization of the upper mantle usually corresponds to low geothermal settings (Friedman et al., 2014). Generally, rift valleys such as the Zhongsha Trough are too hot to form strong mantle magnetism, which is verified by the magnetic data in the northwestern margin (Figure 9a). However, the heat flow values are low along the Zhongjiannan Basin, which may be related to the highly fractured crust. The deep mantle magma accompanying the formation of the oceanic crust could have provided material source for the mantle magnetite.

10.1029/2020TC006260

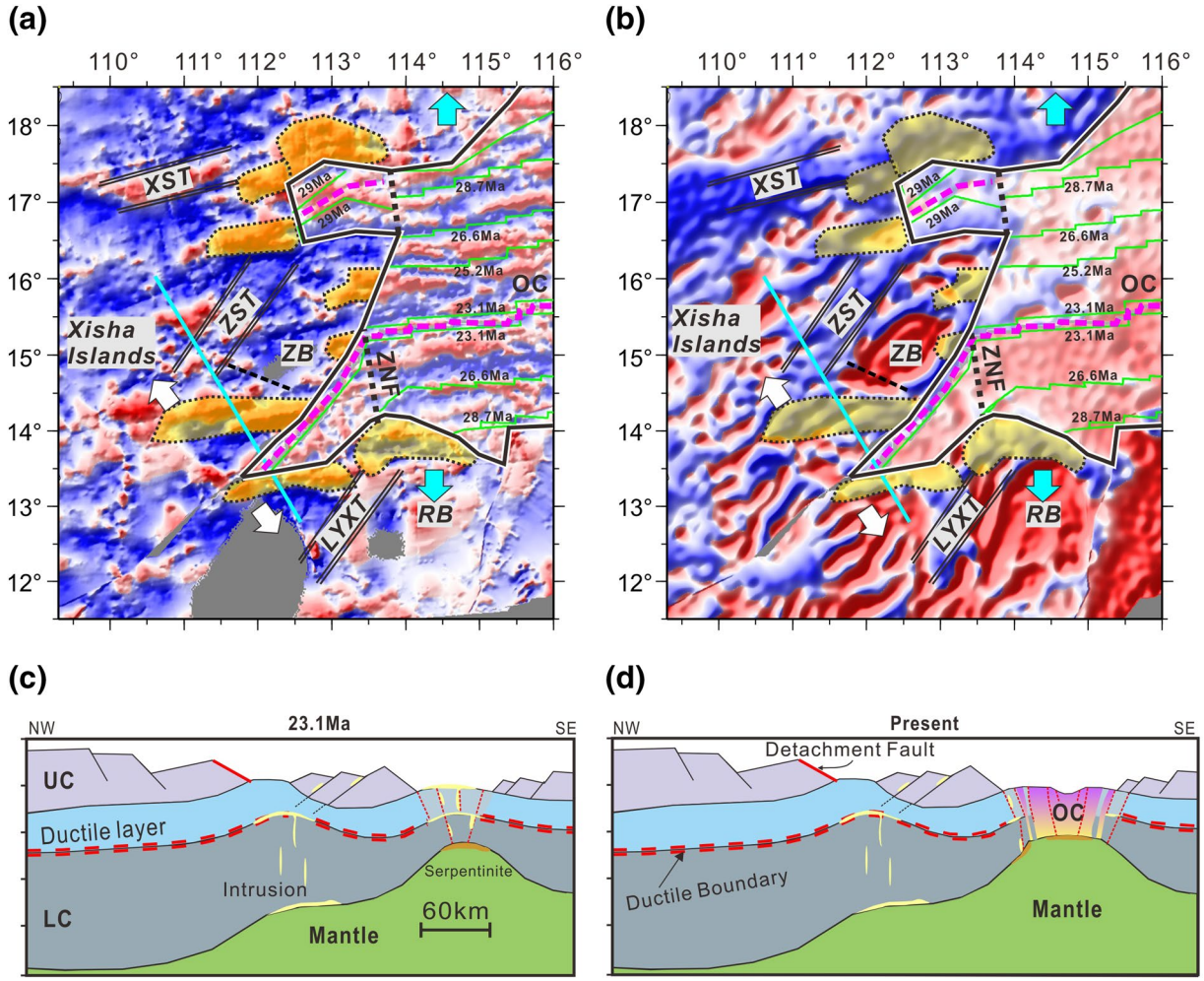

Figure 10. (a) Maps of the magnetic and (b) gravity anomaly of the SCS reconstructed at 23.1 Ma using rotation poles from the GPlates software (Boyden et al., 2011). Yellow areas outlined by dotted lines mask the high magnetic anomaly representing the OCT along the slopes. Green lines are identified magnetic anomalies, representing mature oceanic crust. The blue and white arrows indicate the direction of early and late stages of the seafloor spreading (Briais et al., 1993), respectively. The dashed lines represent the possible strike-slip faults imaged on the Zhongsha Bank (ZB) (X. X. Huang et al., 2020). Dotted lines mark the transform faults identified based on the gravity and magnetic anomalies (Larsen et al., 2018; C. F. Li & Song, 2012). Solid lines denote the reconstructed COB. (c, d) Schematic models for the evolution of the continental margin (c) before and (d) after the seafloor spreading between the Zhongsha Bank (ZB) and the Reed Bank (RB). The location is shown by the blue lines in Figures 10a and 10b. UC, upper crust; LC, lower crust; OC, Oceanic crust.

5.4. Discussion of a Possible Continental Breakup Propagation of Rifting in the NW Margin

From 32 to 23 Ma, the ESB opened in a north-south direction (Figures 10a and 10b), while the continental breakup propagated at a much lower rate from east to west, as suggested by the angle between magnetic anomalies and the rifted margin (Le Pourhiet et al., 2018). Three-dimensional numerical simulations have proposed that far-field compression imposed by gravitational potential from the Indochinese Peninsula could explain the stalled propagation (Jourdon et al., 2020; Le Pourhiet et al., 2018). The ~1000-km-wide west SCS margin formed during this stagnation period, and some rifted structures striking in the direction of the propagation, for example, the Xisha Trough and the ZSNB have been influenced by the stalled E-W propagator. From the velocity model and the compilation in Figure 9, the crust with a thickness of 6–9 km (stretching factor of 3–5) along the OCT regions has a width of less than 50 km, at the scale of the localized deformation as indicated at the propagator tip (Le Pourhiet et al., 2018). The continental margin can also be heavily modified by tectonic structures in front of the propagation, for example, breakup obliquity and transcurrent rifting (Jourdon et al., 2020), during which, the transcurrent rifting evolves as a highly localized crustal-scale strike-slip deformation accompanied by exhumed weak crust. This simulated result

coincides with the observation of an exhumed ductile layer across the Zhongsha Trough. Besides, a short strike-slip fault trending NW-SE can be identified from the reflection seismic data across the Zhongsha Bank (Figure 10; X. X. Huang et al., 2020). We adopt the consideration by Liang et al. (2019) that both detachments along the Zhongsha Trough and the Liyuexi Trough started at the time just before seafloor spreading in the SW subbasin (~23.3 Ma). During the resumed opening of the SWSB, the breakup propagated in the direction rotated by 15° (Sibuet et al., 2016). This obliquity characterizes the rotated basin rifting (Figures 10a and 10b), for example, the E-W direction for ZSNB and Xisha Trough, and NE-SW for the Zhongsha Trough and the Liyuexi Trough.

6. Conclusions

Careful reflection and wide-angle seismic modeling revealed the crustal structures in the NW margin of the SCS. The conclusions are as follows: 1) Crustal deformation was controlled by detachment faults that sole out into a ductile layer at depths of ~7 km below the basement. A sharp velocity boundary exists between this ductile layer and the lower crust in the Zhongsha Trough. 2) The brittle upper crust has detached along a ~20 km wide zone in the Zhongsha Trough, accompanied by thickened lower crust due to magmatic additions. 3) A highly thinned continental crust (~6 km thick) in the Zhongshanan Basin represents the OCT where high magnetic anomaly is related to magmatic addition and upper mantle magnetism. Below the crust, the upper mantle was likely to be partially serpentinized due to short-term fault activity shortly before oceanic spreading. 4) Prominent magmatism at late-stage rifting penetrated the OCT and may have led to a rapid onset of production of proto-oceanic crust.

Data Availability Statement

Data sets for this research are available at the link http://doi.org/10.5281/zenodo.3677587.

Acknowledgments
The NSFC Open Research Cruise (NORC2013-08), funded by the Shiptime Sharing Project of NSFC, has supported the data acquisition of this work. This cruise was conducted onboard R/V "Shiyan 2" by the scientific team and the crew. This study was supported by National Key R&D Program of China [grant number: 2018YFC0309800], National Natural Science Foundation of China [grant numbers: 41676045, 41674092, and 41306046], and Key Special Project for Introduced Talents Team of Southern Marine Science and Engineering Guangdong Laboratory (Guangzhou) [grant number: GML2019ZD0204]. The GMT software (Wessel & Smith, 1995) and Seismic Unix software package (Stockwell, 1999) were used to plot the figures. Many thanks to Native English speaker Alison Chalm for correcting the language. We thank Stephane Operto for providing codes packages of filtering and deconvolution of OBS data. We thank Yao Liang for providing the velocity model of OBS2014s. The discussion with Dr. Dieter Franke greatly improved the manuscript. We thank Matthias Delescluse and two anonymous reviewers for their constructive comments and we also thank the Editor Margaret E. Rusmore.

References

Ao, W., Zhao, M. H., Qiu, X. L., Ruan, A. G., & Li, J. B. (2012). Crustal structure of the northwest sub-basin of the South China Sea and its tectonic implication (in Chinese with English abstract). *Earth Science - Journal of China University of Geosciences*, *37*(4), 779–790.

Bayrakci, G., Minshull, T. A., Sawyer, D. S., Reston, T. J., Klaeschen, D., Papenberg, C., et al. (2016). Fault-controlled hydration of the upper mantle during continental rifting. *Nature Geoscience*, *9*(5), 384–388. https://doi.org/10.1038/NGEO2671

Bosworth, W. (1994). A model for the three-dimensional evolution of continental rift basins, north-east Africa. *Geologische Rundschau*, *83*, 671–688. https://doi.org/10.1007/BF00251067

Boyden, J. A., Müller, R. D., Gurnis, M., Torsvik, T. H., Clark, J. A., Turner, M., et al. (2011). Next-generation plate-tectonic reconstructions using GPlates. In G. R. Keller & C. Baru (Eds.), *Geoinformatics cyber infrastructure for the Solid Earth Sciences* (7, pp. 95–114). Cambridge University Press.

Briais, A., Partriat, P., & Tapponnier, P. (1993). Updated interpretation of magnetic anomalies and seafloor spreading in the South China Sea: Implications for the tertiary tectonics of Southeast Asia. *Journal of Geophysical Research*, *98*(B4), 6299–6328.

Brune, S., Heine, C., Perez-Gussinye, M., & Sobolev, S. V. (2014). Rift migration explains continental margin asymmetry and crustal hyper-extension. *Nature Communications*, *5*, 4014. https://doi.org/10.1038/ncomms5014

Christensen, N. I., & Mooney, W. D. (1995). Seismic velocity structure and composition of the continental crust – A global view. *Journal of Geophysical Research*, *100*(B6), 9761–9788.

Dean, S. M., Minshull, T. A., Whitmarsh, R. B., & Louden, K. E. (2000). Deep structure of the ocean-continent transition in the southern Iberia Abyssal Plain from seismic refraction profiles: The IAM-9 transect at 40 degrees 20'N. *Journal of Geophysical Research*, *105*(B3), 5859–5885.

Deng, H. D., Ren, J. Y., Pang, X., Rey, P. F., McClay, K. R., Watkinson, I. M., et al. (2020). South China Sea documents the transition from wide continental rift to continental break up. *Nature Communications*, *11*, 1–9. https://doi.org/10.1038/s41467-020-18448-y

Ding, W. W., & Li, J. B. (2016). Propagated rifting in the southwest sub-basin, South China Sea: Insights from analogue modelling. *Journal of Geodynamics*, *100*, 71–86. https://doi.org/10.1016/j.jog.2016.02.004

Ferré, E. C., Friedman, S. A., Martín-Hermández, F., Feinberg, J. M., Till, J. L., Ionov, D. A., & Conder, J. A. (2014). Eight good reasons why the uppermost mantle could be magnetic. *Tectonophysics*, *624–625*(11), 3–14. https://doi.org/10.1016/j.tecto.2014.01.004

Franke, D., Savva, D., Pubellier, M., Steuer, S., Mouly, B., Auxietre, J. L., et al. (2014). The final rifting evolution in the South China Sea. *Marine and Petroleum Geology*, *58*, 704–720. https://doi.org/10.1016/j.marpetgeo.2013.11.020

Friedman, S. A., Feinberg, J. M., Ferre, E. C., Demory, F., Martin-Hernandez, F., Conder, J. A., & Rochette, P. (2014). Craton vs. rift uppermost mantle contributions to magnetic anomalies in the United States interior. *Tectonophysics*, *624–625*(11), 15–23. https://doi.org/10.1016/j.tecto.2014.04.023

Fujii, M., Okino, K., Sato, H., Nakamura, K., Sato, T., & Yamazaki, T. (2016). Variation in magnetic properties of serpentinized peridotites exposed on the Yokoniwa Rise, Central Indian Ridge: Insights into the role of magnetite in serpentinization. *Geochemistry, Geophysics, Geosystems*, *17*(12), 5024–5035. https://doi.org/10.1002/2016GC006511

Guo, X. R., Zhao, M. H., Huang, H. B., Qiu, X. L., Wang, J., He, E. Y., & Zhang, J. Z. (2016). Crustal structure of Xisha block and its tectonic attributes (in Chinese with English abstract). *Chinese Journal of Geophysics*, *59*(4), 1414–1425. https://doi.org/10.6038/cjg20160422

Hayes, D. E., & Nissen, S. S. (2005). The South China Sea margins: Implications for rifting contrasts. *Earth and Planetary Science Letters*, *237*(3–4), 601–616. https://doi.org/10.1016/j.epsl.2005.06.017

Henry, W. J., Mechie, J., Maguire, P. K. H., Khan, M. A., Prodehl, C., Keller, G. R., & Patel, J. (1990). A seismic investigation of the Kenya Rift-Valley. *Geophysical Journal International*, *100*(1), 107–130. https://doi.org/10.1111/j.1365-246X.1990.tb04572.x

Hopper, J. R., & Buck, W. R. (1996). The effect of lower crustal flow on continental extension and passive margin formation. *Journal of Geophysical Research*, *101*(B9), 20175–20194. https://doi.org/10.1029/96jb01644

Huang, H. B., Qiu, X. L., Pichot, T., Klingelhoefer, F., Zhao, M. H., Wang, P., & Hao, T. Y. (2019). Seismic structure of the northwestern margin of the South China Sea: Implication for asymmetric continental extension. *Geophysical Journal International*, *218*(2), 1246–1261. https://doi.org/10.1093/gji/ggz219

Huang, H. B., Qiu, X. L., Xu, H. L., Hao, T. Y., Xu, Y., & Li, J. B. (2011). Preliminary results of the earthquake observation and the onshore offshore seismic experiments on Xisha Block. *Chinese Journal of Geophysics*, *54*(6), 1045–1055. https://doi.org/10.1002/cjg2.1683

Huang, X. X., Betzler, C., Wu, S. G., Bernhardt, A., Eagles, G., Han, X. H., & Hovland, M. (2020). First documentation of seismic stratigraphy and depositional signatures of Zhongsha atoll (Macclesfield Bank), South China Sea. *Marine and Petroleum Geology*, *117*, 104349. https://doi.org/10.1016/j.marpetgeo.2020.104349

Huismans, R. S., & Beaumont, C. (2014). Rifted continental margins: The case for depth-dependent extension. *Earth and Planetary Science Letters*, *407*(1), 148–162. https://doi.org/10.1016/j.epsl.2014.09.032

Jian, Z. M., Larsen, H. C., & Alvarez Zarikian, C. A., & The Expedition 368 Scientists. (2018). *Expedition 368 preliminary report: South China Sea rifted margin: International Ocean Discovery Program*. https://doi.org/10.14379/iodp.pr.368.2018

Jin, X. L. (1989). The geosciences research report in South China Sea (in Chinese with English abstract). *Donghai Marine Science*, *7*, 30–42.

Jourdon, A., Le Pourhiet, L., Mouthereau, F., & May, D. A. (2020). Modes of propagation of continental breakup and associated oblique rift structures. *Journal of Geophysical Research: Solid Earth*, *125*, e2020JB019906. https://doi.org/10.1029/2020JB019906

Korenaga, J., Holbrook, W. S., Kent, G. M., Kelemen, P. B., Detrick, R. S., Larsen, H. C., et al. (2000). Crustal structure of the Southeast Greenland margin from joint refraction and reflection seismic tomography. *Journal of Geophysical Research*, *105*(B9), 21591–21614.

Larsen, H. C., Mohn, G., Nirrengarten, M., Sun, Z., Stock, J., Jian, Z., et al. (2018). Rapid transition from continental breakup to igneous oceanic crust in the South China Sea. *Nature Geoscience*, *11*, 782–789. https://doi.org/10.1038/s41561-018-0198-1

Le Pourhiet, L., Chamot-Rooke, N., Delescluse, M., MayWatremez, D. A. L., & Pubellier, M. (2018). Continental break-up of the South China Sea stalled by far-field compression. *Nature Geoscience*, *11*, 605–609. https://doi.org/10.1038/s41561-018-0178-5

Lei, C., & Ren, J. Y. (2016). Hyper-extended rift systems in the Xisha Trough, northwestern South China Sea: Implications for extreme crustal thinning ahead of a propagating ocean. *Marine and Petroleum Geology*, *77*, 846–864. https://doi.org/10.1016/j.marpetgeo.2016.07.022

Lester, R., Van Avendonk, H. J. A., McIntosh, K., Lavier, L., Liu, C. S., Wang, T. K., & Wu, F. (2014). Rifting and magmatism in the northeastern South China Sea from wide-angle tomography and seismic reflection imaging. *Journal of Geophysical Research: Solid Earth*, *119*(3), 2305–2323. https://doi.org/10.1002/2013JB010639

Li, C. F., & Song, T. R. (2012). Magnetic recording of the Cenozoic oceanic crustal accretion and evolution of the South China Sea basin. *Chinese Science Bulletin*, *57*(24), 3165–3181. https://doi.org/10.1007/s11434-012-5063-9

Li, F. C., Sun, Z., Pang, X., Liao, J., Yang, H. F., Xie, H., et al. (2019). Low-viscosity crustal layer controls the crustal architecture and thermal distribution at hyperextended margins: Modeling insight and application to the northern South China Sea margin. *Geochemistry, Geophysics, Geosystems*, *20*, 3248–3267. https://doi.org/10.1029/2019GC008200

Li, F. C., Sun, Z., & Yang, H. F. (2018). Possible spatial distribution of the Mesozoic volcanic arc in the present-day South China Sea continental margin and its tectonic implications. *Journal of Geophysical Research: Solid Earth*, *123*(8), 6215–6235. https://doi.org/10.1029/2017JB014861

Liang, Y., Delescluse, M., Qiu, Y., Pubellier, M., Chamot-Rooke, N., Wang, J., et al. (2019). Décollements, detachments, and rafts in the extended crust of Dangerous Ground, South China Sea: The role of inherited contacts. *Tectonics*, *38*(6), 1863–1883. https://doi.org/10.1029/2018TC005418

Lister, G. S., Etheridge, M. A., & Symonds, P. A. (1986). Detachment faulting and the evolution of passive continental margins. *Geology*, *14*(3), 246–250.

Loureiro, A., Afilhado, A., Matias, L., Moulin, M., & Aslanian, D. (2016). Monte Carlo approach to assess the uncertainty of wide-angle layered models: Application to the Santos Basin, Brazil. *Tectonophysics*, *683*, 286–307. https://10.1016/j.tecto.2016.05.040

Ma, Y. B., Wu, S. G., Lv, F. L., Dong, D. D., Sun, Q. L., Lu, Y. T., & Gu, M. F. (2011). Seismic characteristics and development of the Xisha carbonate platforms, northern margin of the South China Sea. *Journal of Asian Earth Sciences*, *40*(3), 770–783. https://doi.org/10.1190/1.3603660

McIntosh, K., Lavier, L., van Avendonk, H., Lester, R., Eakin, D., & Liu, C. S. (2014). Crustal structure and inferred rifting processes in the northeast South China Sea. *Marine and Petroleum Geology*, *58*, 612–626. https://doi.org/10.1016/j.marpetgeo.2014.03.012

McKenzie, D. (1978). Some remarks on the development of the sedimentary basins. *Earth and Planetary Science Letters*, *40*(1), 25–32.

Mechie, J., Fuchs, K., & Altherr, R. (1994). The relationship between seismic velocity, mineral composition and temperature and pressure in the upper mantle – With an application to the Kenya Rift and its eastern flank. *Tectonophysics*, *236*, 453–464. https://doi.org/10.1016/0040-1951(94)90189-9

Miller, D. J., & Christensen, N. I. (1997). Seismic velocities of lower crustal and upper mantle rocks from the slow spreading Mid-Atlantic Ridge, south of the Kane transform zone (MARK). *Proceedings of the Ocean Drilling Program Scientific Results*, *25*, 763–771.

Mohn, G., ManatschalBeltrando, G. M., Masini, E., & Kusznir, N. (2012). Necking of continental crust in magma-poor rifted margins: Evidence from the fossil Alpine Tethys margins. *Tectonics*, *31*, TC1012. https://doi.org/10.1029/2011TC002961

Nirrengarten, M., Manatschal, G., Tugend, J., Kusznir, N. J., & Sauter, D. (2017). Nature and origin of the J-magnetic anomaly offshore Iberia-Newfoundland: Implications for plate reconstructions. *Terra Nova*, *29*(1), 20–28. https://doi.org/10.1111/ter.12240

Perez-Gussinye, M., & Reston, T. (2001). Rheological evolution during extension at nonvolcanic rifted margins: Onset of serpentinization and development of detachments leading to continental breakup. *Journal of Geophysical Research*, *106*(B3), 3961–3975.

Peron-Pinvidic, G., & Manatschal, G. (2019). Rifted margins: State of the art and future challenges. *Frontiers in Earth Science*, *7*, 218. http://doi.org/10.3389/feart.2019.00218

Pichot, T., Delescluse, M., Chamot-Rooke, N., Pubellier, M., Qiu, Y., & Meresse, F. (2014). Deep crustal structure of the conjugate margins of the SW South China Sea from wide-angle refraction seismic data. *Marine and Petroleum Geology*, *58*, 627–643. http://doi.org/10.1016/j.marpetgeo.2013.10.008

Qiu, N., Wang, Z. F., Xie, H., Sun, Z. P., Wang, Z. W., Sun, Z., & Zhou, D. (2013). Geophysical investigations of crust-scale structural model of the Qiongdongnan Basin, Northern South China Sea. *Marine Geophysical Research*, *34*(3–4), 259–279. http://doi.org/10.1007/s11001-013-9182-8

Qiu, X. L., Ye, S. Y., Wu, S. M., Shi, X. B., Zhou, D., Xia, K. Y., & Flueh, E. R. (2001). Crustal structure across the Xisha Trough, northwestern South China Sea. *Tectonophysics*, *341*, 179–193. http://doi.org/10.1016/s0040-1951(01)00222-0

Ren, J. Y., & Lei, C. (2011). Tectonic stratigraphic framework of Yinggehai-Qiongdongnan Basins and its implication for tectonic province division in South China Sea. *Chinese Journal of Geophysics*, *54*(6), 3303–3314. https://doi.org/10.3969/j.issa.0001-5733.2011.12.028

Rudnick, R. L., & Fountain, D. M. (1995). Nature and composition of the continental crust: A lower crustal perspective. *Reviews of Geophysics*, *33*(3), 267–309. https://doi.org/10.1029/95RG01302

Savva, D., Pubellier, M., Franke, D., Chamot-Rooke, N., Meresse, F., Steuer, S., & Auxietre, J. L. (2014). Different expressions of rifting on the South China Sea margins. *Marine and Petroleum Geology*, *58*, 579–598. https://doi.org/10.1016/j.marpetgeo.2014.05.023

Shi, X. B., Zhou, D., Qiu, X. L., & Zhang, Y. X. (2002). Thermal and rheological structures of the Xisha Trough, South China Sea. *Tectonophysics*, *351*, 285–300. https://doi.org/10.1016/s0040-1951(02)00162-2

Sibuet, J.-C., Yeh, Y. Q., & Li, C. X. (2016). Geodynamics of the South China Sea. *Tectonophysics*, *692*, 98–119. https://doi.org/10.1016/j.tecto.2016.02.022

Stockwell, J. W. (1999). The CWP/SU: Seismic Un*x package. *Computers & Geosciences*, *25*, 415–419.

Sun, Z., Stock, J., Klaus, A., & The Expedition 367 Scientists. (2018). *Expedition 367 preliminary report: South China Sea rifted margin*. International Ocean Discovery Program. https://doi.org/10.14379/iodp.pr.367.2018

Taylor, B., & Hayes, D. E. (1983). *Origin and history of the South China Sea basin*. In D. E. Hayes (Ed.), The tectonic and geologic evolution of Southeast Asia Seas and Islands (*27*, pp. 23–56). Washington, DC: Geophysical Monograph. https://doi.org/10.1029/GM027p0023

Thybo, H., & Nielsen, C. A. (2009). Magma-compensated crustal thinning in continental rift zones. *Nature*, *457*, 873–876. https://doi.org/10.1038/nature07688

Wan, K. Y., Xia, S. H., Cao, J. H., Sun, J. L., & Xu, H. L. (2017). Deep seismic structure of the northeastern South China Sea: Origin of a high-velocity layer in the lower crust. *Journal of Geophysical Research: Solid Earth*, *122*(4), 2831–2858. https://doi.org/10.1002/2016JB013481

Wang, Q., Zhao, M. H., Zhang, H. Y., Zhang, J. Z., He, E. Y., Yuan, Y., & Qiu, X. L. (2020). Crustal velocity structure of the Northwest Sub-basin of the South China Sea based on seismic data reprocessing. *Science China Earth Sciences*, *63*, 1791–1806. https://doi.org/10.1007/s11430-020-9654-4

Wernicke, B. (1981). Low-angle normal faults in the Basin and range province: Nappe tectonics in an extending orogen. *Nature*, *291*, 645–648.

Wessel, P., & Smith, W. H. F. (1995). New version of the generic mapping tools. *Eos*, *76*(33), 329–336. https://doi.org/10.1029/95EO00198

West, M., Menke, W., Tolstoy, M., Webb, S., & Sohn, R. (2001). Magma storage beneath axial volcano on the Juan de Fuca mid-ocean ridge. *Nature*, *413*, 833–836. https://doi.org/10.1038/35101581

White, R., & McKenzie, D. (1989). Magmatism at rift zones: The generation of volcanic continental margins and flood Basalts. *Journal of Geophysical Research*, *94*(B6), 7685–7729.

White, R. S., McKenzie, D., & Onions, R. K. (1992). Oceanic crustal thickness from seismic measurements and rare earth element inversions. *Journal of Geophysical Research*, *97*(B13), 19683–19715.

Whitmarsh, R. B., Pinheiro, L. M., Miles, P. R., & Sibuet, J. C. (1993). Thin crust at the western Iberia Ocean-Continent transition and ophiolites. *Tectonics*, *12*(5), 1230–1239.

Wu, Z. L., Li, J. B., Ruan, A. G., Lou, H., Ding, W. W., Niu, X. W., & Li, X. B. (2011). Crustal structure of the northwestern sub-basin, South China Sea: Results from a wide-angle seismic experiment (in Chinese with English abstract). *Science China Earth Sciences*, *41*(10), 1463–1476. https://doi.org/10.1007/s11430-011-4324-9

Yan, P., Zhou, D., & Liu, Z. (2001). A crustal structure profile across the northern continental margin of the South China Sea. *Tectonophysics*, *338*(1), 1–21.

Yu, J. H., Yan, P., Wang, Y. L., Zhang, J. C., Qiu, Y., Pbuellier, M., & Delescluse, M. (2018). Seismic evidence for tectonically dominated seafloor spreading in the Southwest Sub-basin of the South China Sea. *Geochemistry, Geophysics, Geosystems*, *19*(9), 3459–3477. https://doi.org/10.1029/2018GC007819

Zelt, C. A., & Ellis, R. M. (1988). Practical and efficient ray tracing in two-dimensional media for rapid traveltime and amplitude forward modeling. *Canadian Journal of Exploration Geophysics*, *24*(1), 16–31.

Zelt, C. A., & Smith, R. B. (1992). Seismic traveltime inversion for 2-D crustal velocity structure. *Geophysical Journal International*, *108*(1), 16–34. https://doi.org/10.1111/j.1365-246X.1992.tb00836.x

Zhang, M. S. (1991). Quaternary events in Xisha coral reef region (in Chinese with English abstract). *Quaternary Sciences*, *2*, 165–177.

Zhang, J., Li, J. B., Ruan, A. G., Wu, Z. L., Yu, Z. T., Niu, X. W., & Ding, W. W. (2016a). The velocity structure of a fossil spreading centre in the southwest sub-basin, South China Sea. *Geological Journal*, *51*(S1), 548–561. https://doi.org/10.1002/gj.2778

Zhang, Q., Wu, S. G., & Dong, D. D. (2016b). Cenozoic magmatism in the northern continental margin of the South China Sea: Evidence from seismic profiles. *Marine Geophysical Researches*, *37*(2), 71–94. https://doi.org/10.1007/s11001-016-9266-3

Zhao, M. H., He, E. Y., Sibuet, J. C., Sun, L. T., Qiu, X. L., Tan, P. C., & Wang, J. (2018). Postseafloor spreading volcanism in the central east South China Sea and its formation through an extremely thin oceanic crust. *Geochemistry, Geophysics, Geosystems*, *19*(3), 621–641. https://doi.org/10.1002/2017GC007034

Zhu, J. J., Li, J., Sun, Z. X., & Li, S. Z. (2016). Crustal thinning and extension in the northwestern continental margin of the South China Sea. *Geological Journal*, *51*(S1), 286–303. https://doi.org/10.1002/gj.2753

Zhu, W. L., Xie, X. N., Wang, Z. F., Zhang, D. J., Zhang, C. L., Cao, L. C., & Shao, L. (2017). New insights on the origin of the basement of the Xisha Uplift, South China Sea. *Science China Earth Sciences*, *60*, 2214–2222. https://doi.org/10.1007/s11430-017-9089-9